nature nanotechnology

ARTICLES

https://doi.org/10.1038/s41565-019-0429-7

Current-controlled propagation of spin waves in antiparallel, coupled domains

Chuanpu Liu[1,12], Shizhe Wu[2,12], Jianyu Zhang[1,12], Jilei Chen[1,12], Jinjun Ding[3,12], Ji Ma[4,12], Yuelin Zhang[2], Yuanwei Sun[5], Sa Tu[1], Hanchen Wang[1], Pengfei Liu[6], Chexin Li[6], Yong Jiang[6], Peng Gao[5], Dapeng Yu[5,7], Jiang Xiao[8,9], Rembert Duine[10,11], Mingzhong Wu[3], Ce-Wen Nan[4], Jinxing Zhang[2]* and Haiming Yu[1]*

Spin waves may constitute key components of low-power spintronic devices. Antiferromagnetic-type spin waves are innately high-speed, stable and dual-polarized. So far, it has remained challenging to excite and manipulate antiferromagnetic-type propagating spin waves. Here, we investigate spin waves in periodic 100-nm-wide stripe domains with alternating upward and downward magnetization in $La_{0.67}Sr_{0.33}MnO_3$ thin films. In addition to ordinary low-frequency modes, a high-frequency mode around 10 GHz is observed and propagates along the stripe domains with a spin-wave dispersion different from the low-frequency mode. Based on a theoretical model that considers two oppositely oriented coupled domains, this high-frequency mode is accounted for as an effective antiferromagnetic spin-wave mode. The spin waves exhibit group velocities of 2.6 km s^{-1} and propagate even at zero magnetic bias field. An electric current pulse with a density of only 10^5 A cm^{-2} can controllably modify the orientation of the stripe domains, which opens up perspectives for reconfigurable magnonic devices.

Spin waves[1–4] may enable low-power-consumption spin information transmission that is free of Joule heating[5,6] and can be reconfigurable[7,8]. Antiferromagnetic (AFM) spin waves have intrinsic advantages, such as high speed, dual polarization and immunity to external field perturbation[9,10]. However, AFM spin waves are very difficult to excite and to probe, let alone to integrate on-chip for applications, due to their high frequency in the sub-terahertz to terahertz regime[11,12]. Synthetic AFM structures[13] may provide an opportunity to realize and utilize AFM-type spin waves[14,15], and opening the bandgaps of artificial magnonic crystals has been studied in AFM-order nanowire arrays using spin-wave reflection spectra[16,17]. It is of great importance to realize current-control propagation of spin waves for reconfigurable magnonic devices[18,19]. However, to excite AFM-type spin waves and to control their propagation with current remain a major challenge in the fields of magnonics and spintronics.

$La_{0.67}Sr_{0.33}MnO_3$ (LSMO) thin films, with naturally formed periodic 100-nm-wide stripe domains[20,21], provide an ideal platform to study AFM-type spin-wave propagation. In this Article we use integrated coplanar waveguides (CPWs) with a 260-nm-wide signal line to excite and detect effective AFM spin waves, that is, spin waves in an artificial antiferromagnet where the coupled upward and downward domains in the LSMO are regarded as two sublattices. Transmission signals are detected for effective AFM spin waves in the absence of a magnetic field. The group velocity is estimated to reach 2.6 km s^{-1}, substantially higher than the velocities of domain wall motion (0.75 km s^{-1} or 1.7 km s^{-1})[22,23] and skyrmion motion (0.1 km s^{-1})[24]. The AFM-type spin waves propagate at high frequencies (~10 GHz) in the domain volume, whereas ferromagnetic-type spin waves propagate at lower frequencies (~2 GHz) in the domain wall[8]. We experimentally demonstrate that the one-dimensional AFM-order stripe domains acting as spin-wave channels can be rewritten by a pulsed direct current and achieve reconfigurable AFM-type spin-wave propagation.

Spin-wave propagation in 100-nm periodic domain stripes

Figure 1a shows spin-wave propagation in periodic multidomain stripes of an LSMO film, which is perpendicularly magnetized and antiferromagnetically ordered with a periodicity of ~220 nm. The 150-nm-thick LSMO film was grown on a $LaAlO_3$ (LAO) substrate by pulsed laser deposition[25] (see Methods). Lattice mismatch between the LSMO (cubic 3.86 Å) and LAO (cubic 3.80 Å) gives rise to an out-of-plane magnetic anisotropy[26]. Figure 1c presents a high-angle annular dark-field image of the LSMO on LAO (see Supplementary Fig. 1 for the lattice constant measurements). The film was initially saturated by applying an in-plane field of 150 mT for 1 s. The field was then turned off and the magnetization in the film relaxed to form periodic stripe domains with alternating upward and downward domains. The domain stripes were found to align along the orientation of the initial field. The micromagnetic simulations indicate a vortex wall texture as shown in Fig. 1b, consistent with those reported previously[17,27]. Figure 1d,e presents magnetic force microscope (MFM) data. The MFM results show that the domain width is ~90 nm and the wall width is ~20 nm. Figure 1f

[1]Fert Beijing Institute, BDBC, School of Microelectronics, Beihang University, Beijing, China. [2]Department of Physics, Beijing Normal University, Beijing, China. [3]Department of Physics, Colorado State University, Fort Collins, CO, USA. [4]State Key Lab of New Ceramics and Fine Processing, School of Materials Science and Engineering, Tsinghua University, Beijing, China. [5]State Key Laboratory for Mesoscopic Physics and Electron Microscopy Laboratory, School of Physics, Peking University, Beijing, China. [6]Beijing Advanced Innovation Center for Materials Genome Engineering, School of Materials Science and Engineering, University of Science and Technology Beijing, Beijing, China. [7]Department of Physics, Southern University of Science and Technology, Shenzhen, China. [8]Department of Physics and State Key Laboratory of Surface Physics, Fudan University, Shanghai, China. [9]Collaborative Innovation Center of Advanced Microstructures, Nanjing, China. [10]Institute for Theoretical Physics, Universiteit Utrecht, Utrecht, the Netherlands. [11]Department of Applied Physics, Eindhoven University of Technology, Eindhoven, the Netherlands. [12]These authors contributed equally: Chuanpu Liu, Shizhe Wu, Jianyu Zhang, Jilei Chen, Jinjun Ding, Ji Ma. *e-mail: jxzhang@bnu.edu.cn; haiming.yu@buaa.edu.cn

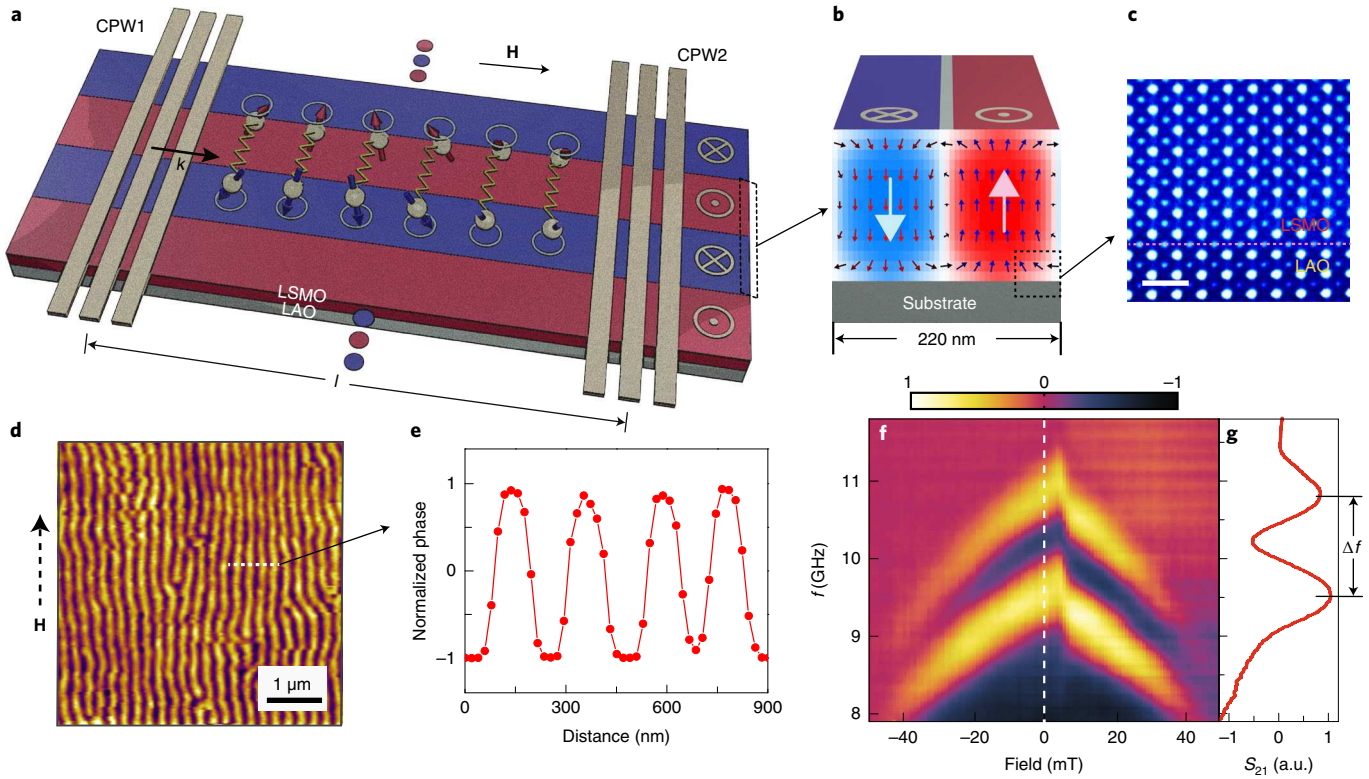

Fig. 1 | Nanostripe domain structures and spin-wave spectra measured by a VNA. a, Sketch of a perpendicularly magnetized LSMO thin film with alternating upward (red) and downward (blue) domains. The CPWs are integrated on the top to excite and detect spin waves. The spin-wave wavevector **k** is parallel to the domain stripes. The field **H** is applied along the domain stripes. **b**, Magnetic textures in the domain wall cross-section from micromagnetic simulations. **c**, A high-angle annular dark-field image of the LSMO on top of the LAO substrate. Scale bar, 1 nm. **d**, Out-of-plane magnetization mapped by MFM at zero applied field. An external field **H** was initially set at 150 mT along the vertical orientation indicated by the dashed arrow and then removed during the MFM measurement. **e**, Lineplot of the MFM results at the position indicated by the white dashed line in **d** showing that the domain width is ~90 nm and the domain wall width is ~20 nm. **f**, Colour-coded transmission spectra S_{21} measured as the imaginary part from the VNA on the nanostripe domain device shown in **a**. **g**, A single spin-wave spectrum extracted at zero magnetic field.

presents spin-wave transmission spectra S_{21} (spin waves excited by CPW1 and detected by CPW2) measured by a vector network analyser (VNA) as a function of the bias field. The field was applied parallel to the wavevector **k**. The field was initially set to −150 mT to saturate the film and then gradually increased. The stripe domains were formed from around −50 mT (Supplementary Fig. 2). The field was then swept from −50 mT to 50 mT in 1 mT steps. Spin-wave spectra (for example, Fig. 1g) were measured at each field and plotted together as the colour-coded spectra in Fig. 1f. A clear spin-wave phase oscillation is observed, indicating coherent spin-wave propagation[28–30]. The propagation distance is ~2 μm. The spin-wave spectrum at zero magnetic field is shown in Fig. 1g. The peak-to-peak frequency span Δf suggests a phase delay $\Delta\phi = 2\pi$, and therefore the spin-wave group velocity is estimated to be ~2.6 km s^{-1} based on

$$v_g = \frac{d\omega}{dk} \approx \frac{2\pi\Delta f}{2\pi/l} = \Delta f \times l \quad (1)$$

where l is the propagation distance. A sharp frequency shift is observed in the spin-wave spectra shown in Fig. 1f around 6 mT. The micromagnetic simulations suggest a magnetization switching at the core of the vortex domain wall[31].

The spin-wave reflection measurements were conducted using a conventional CPW flip-chip technique (see Methods). A high-frequency mode is observed in the reflection spectra S_{11} (Fig. 2a) on top of a low-frequency ferromagnetic resonance mode. To study the origin of these different resonance modes, we performed micromagnetic simulations (see Methods) based on the object oriented micromagnetic framework (OOMMF)[27]. The field was applied in plane and parallel to the domain stripe for both experiments and simulations. Figure 2b shows the simulated reflection spectra in the same field range of Fig. 2a. The high-frequency (HF) and low-frequency (LF) branches are around 8 GHz and 2 GHz, respectively, in the simulated spectra. The dynamic magnetization landscapes of these two modes are shown in Fig. 2d,e at zero field. The HF spin waves can propagate over a substantially longer distance than the LF spin waves along the stripe domains, based on the simulation results. For the experimental results shown in Fig. 1f, the distance between two antennas is 2 μm, and therefore only the spin-wave propagation of the HF mode is observed. The reflection spectra for different locations of the multidomain film were simulated (Fig. 2f–h). The simulation results are consistent with a recent study on Fe–N films where multimodes are observed with a distinctive spatial localization in specific regions[32]. The LF spin waves are observed both in the domain walls and at the domain surface. However, the HF spin waves are observed only in the domain volume. These micromagnetic simulations reveal that the propagating spin waves observed in Fig. 1f are primarily localized in the domain volume. The simulation results are partially supported by the experimental observations in Fig. 2a where the HF and LF modes exhibit different field dependence, because the applied in-plane field is along the easy axis for LF modes (mostly in-plane) and along the hard axis for HF modes (mostly out-of-plane).

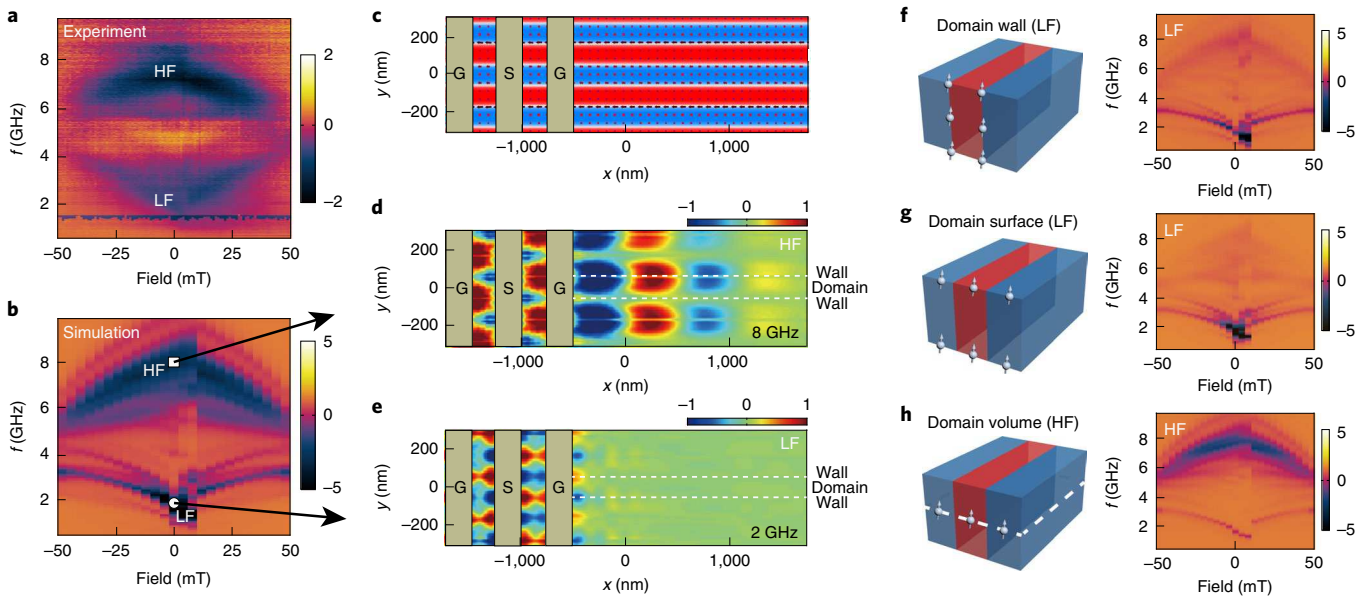

Fig. 2 | Spin-wave reflection measurement and micromagnetic simulations. a, Colour-coded spin-wave reflection spectra S_{11} of an LSMO thin film measured using the CPW flip-chip method showing both high-frequency (HF) and low-frequency (LF) modes. The field was swept from −50 mT to 50 mT with a field step of 1 mT. **b**, Simulated spin-wave spectra on the LSMO nanostripe domain sample as a function of external field. **c**, Simulated micromagnetic landscape showing a horizontal alignment of stripe domains. The spin waves were excited by a ground–signal–ground (G–S–G) CPW. Red and blue pixels correspond to $+M_z$ and $-M_z$, respectively. **d**,**e**, Spatial mapping of propagating spin-wave intensity for HF modes around 8 GHz (**d**) and LF modes around ~2 GHz (**e**). The colour scale in **d** and **e** represents the x component of the magnetization (m_x). The excitation antenna is located in the centre and has a width of 100 nm. **f**–**h**, Simulated spin-wave spectra analysed at the domain walls (**f**), domain surface (**g**) and in the domain volume (**h**).

Spin waves controlled by reconfigurable domain stripes

Figure 3a shows the MFM images of magnetic domain patterns. One can rotate the stripe domain alignment by applying an external magnetic field of 150 mT with different angle θ (Fig. 3a–d)[17]. The spin-wave transmission spectra S_{21} at zero field are presented in Fig. 3e–h with rotating domain stripe orientations. The spin-wave transmission amplitude decreases dramatically when the domain stripes rotate from 0° to 90° as shown in Fig. 3j (the method for amplitude and frequency extraction from raw data is shown in Supplementary Fig. 3). These observations indicate that spin waves tend to propagate along domain stripes and are strongly attenuated if **k** is perpendicular to the domain stripes[33,34], which is also supported by the micromagnetic simulations with tilted domain stripes (Supplementary Fig. 4). The excitation efficiency with respect to θ is found to be slightly varied and is characterized by the spin-wave reflection measurement S_{11} (Supplementary Fig. 5). The angle dependence of spin-wave transmission amplitude can be explained as the variation of propagation distance while changing the domain stripe alignment as $l_\theta = l/\cos\theta$. The transmission signal amplitude S_{21} can be written as $S_{21} = \frac{1}{2}S_{11}\exp(-l_\theta/l_d)$, where S_{11} is the reflection signal amplitude and l_d is the spin-wave decay length[35] characterizing the exponential decay of the amplitude. The spin-wave propagation distance $l = 2\,\mu$m. After normalization of the signal amplitude at $\theta = 180°$ as 100%, we fit the angle dependence of the relative spin-wave amplitude (Fig. 3j) and derive a spin-wave decay length of 830 nm, taking into account the angle dependence of the excitation efficiency. Such behaviour enables the control of spin-wave propagation by rotating domain stripes. The resonance frequency also varies slightly with the stripe orientations and reaches maxima when **k** is parallel to the domain stripes (Fig. 3k), showing comparable spin-wave resonance frequency for S_{11} at the excitation region. The plane-wave band structures[36] show weak anisotropy, in good agreement with the experimental results (Supplementary Fig. 5). The frequency variation is understandable if we consider an effective wavevector $\mathbf{k}_{||}$ along the domain stripe that is angle-dependent, as shown in Fig. 3b, and therefore contributes differently to the dispersion according to equation (7) (see later).

Magnetization measurements on the LSMO film were carried out with out-of-plane (Fig. 4a) and in-plane (Fig. 4b) applied fields. The ferromagnetic resonances (FMRs) were measured with an in-plane field. The fitting in Fig. 4c yields an effective saturation magnetization $M_S = 307 \pm 29\,\mathrm{kA\,m^{-1}}$ and an absolute gyromagnetic ratio $|\gamma/2\pi| = 28.8 \pm 0.9\,\mathrm{GHz\,T^{-1}}$. The anisotropy field $\mu_0 H_{ani} = 75$ mT is extracted from magnetization measurements (Fig. 4a,b). The effective Gilbert damping parameter $\alpha = 0.034$ is estimated by fitting the frequency-dependent linewidth (Fig. 4d). The fine step at low fields in both the in-plane and out-of-plane configurations (insets of Fig. 4a,b) may be induced by core switching in the vortex domain-wall texture[31]. This observation indicates the presence of Dzyaloshinskii–Moriya interactions (DMIs) in the magnetic texture[37]. A small DMI is estimated from spin-wave non-reciprocity measurements[38] with an in-plane field perpendicular to the wavevector **k** (Supplementary Fig. 6). The DMI could then be responsible for the slight deviation from 180° for both the amplitude (Fig. 3j) and frequency (Fig. 3k). The origin of the DMI is probably the substrate-induced strain at the LAO/LSMO interface that creates symmetry breaking in the out-of-plane orientation. The 10 GHz spin-wave resonance frequency at zero magnetic field (Fig. 1e) is high compared to the FMR mode of a film with a single domain, which exhibits a resonance frequency of ~2 GHz.

Modelling of the effective AFM spin-wave mode

We now turn to a physical interpretation of the HF mode: spin waves propagating in upward and downward domains are not independent but are strongly coupled and therefore form a collective spin-wave mode as shown in Fig. 1a. We start from a simplified model to study spin waves along two coupled domains. We consider two oppositely oriented domains with magnetization direction

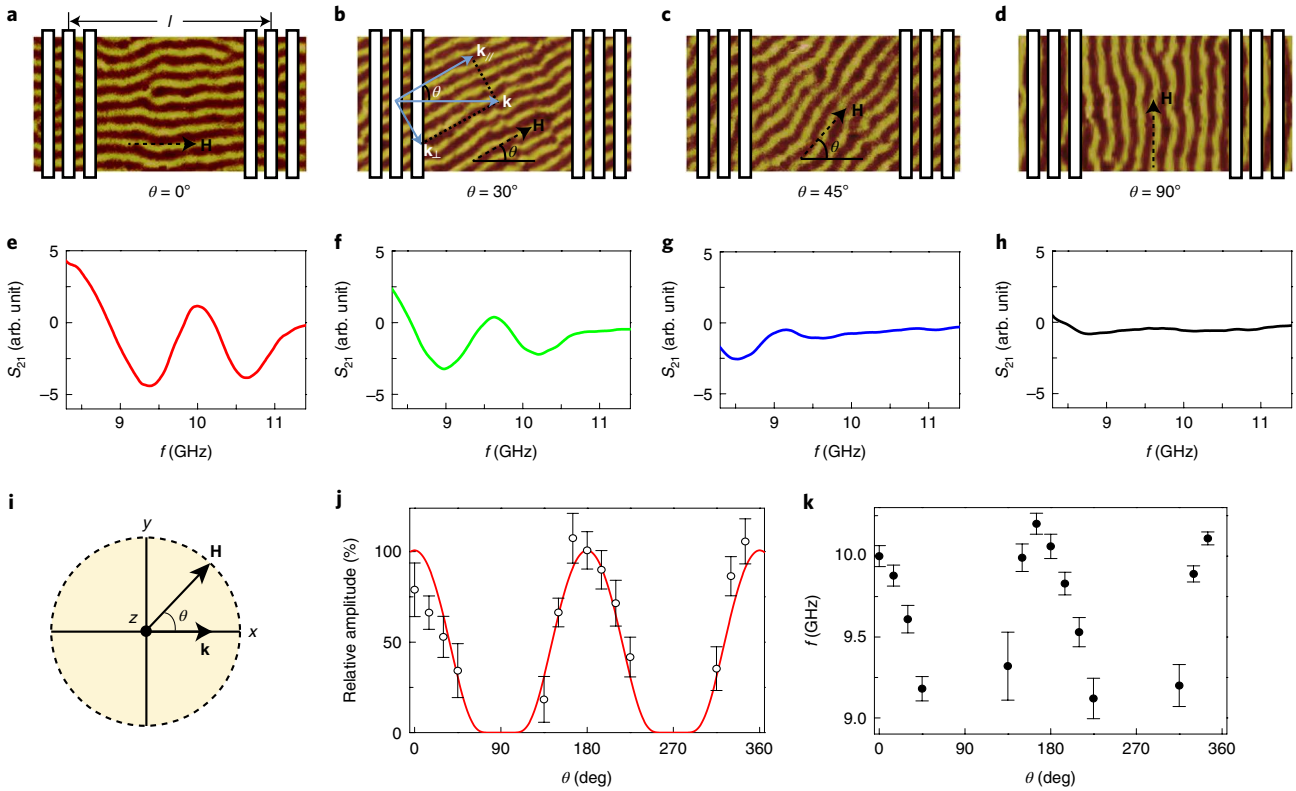

Fig. 3 | Control spin-wave propagation by rotating domain stripes. a–d, MFM imaging of an LSMO film with different domain stripe orientations 0° (**a**), 30° (**b**), 45° (**c**) and 90° (**d**). An external field of 150 mT was applied for 1 s at the angle θ and then turned off to reorient the stripe domains along the field. **e–h**, Spin-wave transmission spectra S_{21} at zero magnetic field with $\theta = 0°$ (**e**), 30° (**f**), 45° (**g**) and 90° (**h**). **i**, θ is defined as the angle between spin-wave wavevector **k** and the external magnetic field used to align the domain stripes. **j**, Amplitude of spin-wave transmission as a function of θ. The largest amplitude is normalized as 100%. The red curve is a fit based on numerical calculation. Error bars indicate the uncertainty of relative amplitude of spin-wave transmission. **k**, Spin-wave frequency f as a function of θ. Error bars are based on the uncertainty of frequency determination.

along the z axis, as shown in the inset (top view) of Fig. 4e. We take into account an out-of-plane anisotropy so that the energy is

$$E = \int \frac{\mathrm{d}^3\mathbf{r}}{a^3}\left\{-\frac{J}{2}\mathbf{m}_\uparrow\cdot\nabla^2\mathbf{m}_\uparrow - \frac{J}{2}\mathbf{m}_\downarrow \cdot\nabla^2\mathbf{m}_\downarrow - \frac{K}{2}m_{\uparrow,z}^2 - \frac{K}{2}m_{\downarrow,z}^2 + J_{\uparrow\downarrow}\mathbf{m}_\uparrow\cdot\mathbf{m}_\downarrow\right\} \quad (2)$$

where J is the ordinary exchange constant, K is the anisotropy constant and $J_{\uparrow\downarrow}$ is the coupling between domains. Then the Landau–Lifshitz–Gilbert equations are given by

$$\begin{cases}\dfrac{\partial\mathbf{m}_\uparrow}{\partial t} = J\mathbf{m}_\uparrow\times\nabla^2\mathbf{m}_\uparrow + K\mathbf{m}_\uparrow\times m_{\uparrow,z}\hat{\mathbf{z}} - J_{\uparrow\downarrow}\mathbf{m}_\uparrow\times\mathbf{m}_\downarrow + \alpha\mathbf{m}_\uparrow\times\dfrac{\partial\mathbf{m}_\uparrow}{\partial t} \\ \dfrac{\partial\mathbf{m}_\downarrow}{\partial t} = J\mathbf{m}_\downarrow\times\nabla^2\mathbf{m}_\downarrow + K\mathbf{m}_\downarrow\times m_{\downarrow,z}\hat{\mathbf{z}} - J_{\mathrm{aa}\uparrow\downarrow}\mathbf{m}_\downarrow\times\mathbf{m}_\uparrow + \alpha\mathbf{m}_\downarrow\times\dfrac{\partial\mathbf{m}_\downarrow}{\partial t}\end{cases} \quad (3)$$

In the antiparallel configuration, we write

$$\mathbf{m}_\uparrow = \begin{pmatrix}\delta A_x\\ \delta A_y\\ 1\end{pmatrix}, \mathbf{m}_\downarrow = \begin{pmatrix}\delta B_x\\ \delta B_y\\ -1\end{pmatrix} \quad (4)$$

We now linearize for small δA and δB, make a plane wave ansatz, and solve the 4×4 matrix resulting from equation (3), which yields

$$\omega \to \mp\sqrt{Jk^2+K}\sqrt{2J_{\uparrow\downarrow}+Jk^2+K} \quad (5)$$

where k is the spin-wave wavevector. The detailed calculations are presented in Supplementary Section H. We now take the positive frequency solution and rewrite it with variables of the same units studied in experiments as

$$\omega = \gamma\mu_0\sqrt{(H_{\mathrm{ani}}+M_S\lambda_{\mathrm{ex}}k^2)(H_{\mathrm{ani}}+2H_{\mathrm{eff}}^{\uparrow\downarrow}+M_S\lambda_{\mathrm{ex}}k^2)} \quad (6)$$

where H_{ani} is the anisotropy field, λ_{ex} is the exchange constant of LSMO and $H_{\mathrm{eff}}^{\uparrow\downarrow}$ is the effective coupling field between upward and downward domains. This dispersion relation is similar to the AFM resonance $\omega = \gamma\mu_0\sqrt{H_{\mathrm{ani}}(H_{\mathrm{ani}}+2H_{\mathrm{E}})}$ (ref. [39]) if one considers the condition $k = 0$, except that the $H_{\mathrm{eff}}^{\uparrow\downarrow}$ in the LSMO is the coupling between upward and downward domains and H_{E} is the exchange field between spins of two sublattices. In an actual antiferromagnet, the modes are pushed up to high frequencies by the exchange interactions, resulting in 'exchange-enhanced' frequencies. Here, it is the interdomain coupling that pushes them up. Therefore, we refer to this high-frequency mode as an effective AFM spin-wave mode. Now, we use equation (6) to determine the spin-wave dispersion and compare with experimental data. Considering the wavevector k induced by CPW is in the range of a few rad μm^{-1}, the dipolar spin-

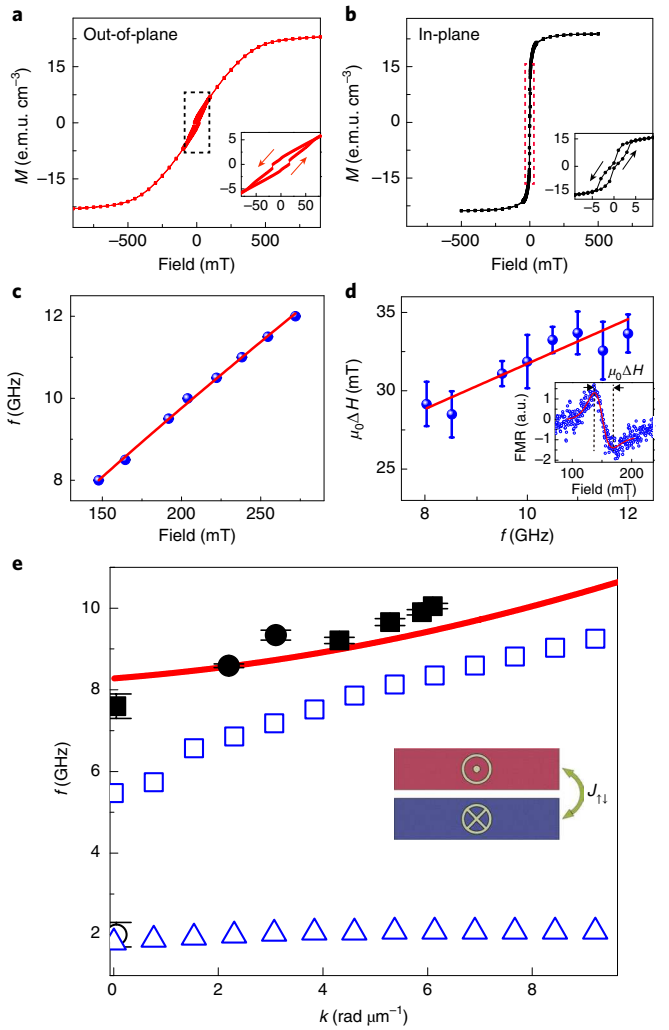

Fig. 4 | Magnetic characterization and spin-wave dispersion relations. **a**,**b**, Magnetic hysteresis loops measured in a superconducting quantum interference device (SQUID) with out-of-plane (**a**) and in-plane (**b**) fields on the LSMO thin film. Insets, data at the low-field range. **c**, Ferromagnetic resonance frequencies f as a function of in-plane applied field H. The red line is a numerical fit to the Kittel formula. **d**, Ferromagnetic resonance linewidth ΔH as a function of resonance frequency f. Error bars indicate the uncertainty of the linewidth extraction from FMR spectra, as shown in the inset at 8 GHz, for example. **e**, Spin-wave dispersion relations. Data points (black filled squares, sample A; black filled circles, sample B) are extracted from transmission spectra S_{21} with wavevector $k = k_0 \cos\theta$ where $\theta = 0°$, 15°, 30° and 45°. Error bars indicate the uncertainty of frequency determination. The red curve shows the calculated dispersion relation based on the analytical theory on spin waves along the coupled domains. Blue open squares (HF mode) and blue open triangles (LF mode) are extracted from the micromagnetic simulations.

wave contribution to the spin-wave dispersion is not negligible. Therefore, we add a forward-volume magnetostatic spin-wave term in the dispersion[40,41] and obtain

$$\omega = \gamma\mu_0 \left[(H_{ani} + M_S \lambda_{ex} k^2) \left(H_{ani} + 2H_{eff}^{\uparrow\downarrow} + M_S \lambda_{ex} k^2 + M_S \left(1 - \frac{1 - e^{-kd}}{kd} \right) \right) \right]^{1/2} \quad (7)$$

Here, d is the film thickness. We take H_{ani} and M_S from SQUID and FMR characterization (Fig. 4a–d) and $\lambda_{ex} = 1.37 \times 10^{-16}$ m^2 from ref. [27]. The wavevector k (x axis in Fig. 4e) varies with θ following $k = k_0 \cos\theta$. Here, $k_0 = 6.1$ rad μm^{-1} (sample A) and 3.1 rad μm^{-1} (sample B, Supplementary Fig. 7) are calculated from the Fourier transformation of the CPWs[30]. The group velocities $v_g = \frac{d\omega}{dk}$ extracted from the micromagnetic simulations are 1.36 km s^{-1} for the HF mode and 0.19 km s^{-1} for the LF mode, which explains why the HF mode can propagate further than the LF mode (Fig. 2d,e). To fit these experimental results, we use equation (7) and take the interdomain effective coupling field $\mu_0 H_{eff}^{\uparrow\downarrow} = 550$ mT. The dipolar coupling is considered to be mainly responsible for the effective coupling between neighbouring domains[42]. The frequency blue-shift induced by interdomain dipolar coupling is estimated to be ~3.1 GHz without considering any dynamic exchange through the domain-wall texture (Supplementary Section I). Because dipolar interactions are proportional to the saturation magnetization, materials such as CoFeB[43,44] can reach even higher frequencies with the same domain stripes. The effective AFM spin waves observed in this work are in analogy to the spin waves studied in multilayers with AFM couplings[14,15], but the in-plane periodic domains instead of out-of-plane multilayers offer the possibility to rotate the domain stripes with an electric current (Fig. 5) to achieve reconfigurable magnonic devices.

Current control of spin waves in nanostripe domains

The studied device is shown in Fig. 5a, where the electrical contacts for direct current were integrated on an LSMO crossbar. The domain stripes were initially aligned in the x direction, as shown in Fig. 5b, and the current pulse was also applied in the x direction. The MFM images of the domain stripe pattern are shown in Fig. 5c–e after current pulses of 10 μs with magnitude of 10 mA, 20 mA and 25 mA, respectively. The domain stripes remained unchanged up to 20 mA, but were reoriented with an applied current of 25 mA. The domain stripes preferred to reorient perpendicular to the current direction. The current-switching mechanism may originate from spin-transfer torque (STT)[45,46] and spin–orbit torque (SOT)[47,48] effects. From experimental results on an eight-terminal LSMO device (Supplementary Fig. 9), the current-switching behaviour is found to be strongly anisotropic depending on the current injection with respect to the crystalline orientations. Therefore, the main switching mechanism in this planar geometry is considered to be SOT, which may stem from the inversion asymmetry induced by the strain[49] from the substrate at the LSMO/LAO interface, as shown in Fig. 1c and Supplementary Fig. 1. Considering that an applied field can align the domain stripes in analogy to the applied current as shown in Fig. 3a–d, we assume that the field-like SOT[48] may be mainly responsible for the observation. However, the STT can also contribute when current is driven through the domain texture. A full spin-wave transmission spectrum S_{21} is shown in Supplementary Fig. 10. Sizable spin-wave transmission signals are observed at the initial state, as shown in Fig. 5g, and maintain a similar amplitude after current pulses of 10 mA and 20 mA, where the domain stripes are yet to switch. However, as soon as a current pulse of 25 mA is applied, the spin-wave transmission signal disappears, as a result of the domain stripe reorientation. These results demonstrate experimentally the possibility to switch the spin-wave transmission from 'on' to 'off' using a current pulse. The threshold switching current density is only 1.7×10^5 A cm^{-2}, which is approximately two orders of magnitude lower than magnetic multilayer switching[45,47]. The ultralow current density needed for switching the domain stripe alignment of the LSMO is consistent with the low applied field needed to reorient the domain stripes—found to be ~40 mT for LSMO[27] (80 mT for FeGa domain stripes[50]). This indirectly supports the argument that the field-like SOT is the main current-switching mechanism.

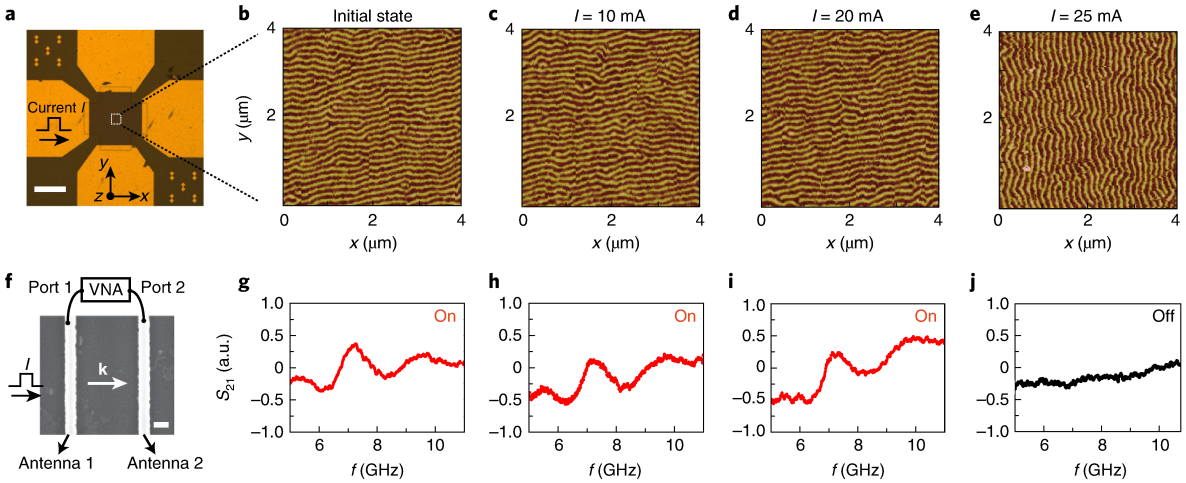

Fig. 5 | Current switching of the stripe domains for reconfigurable spin-wave propagation. a, Optical microscopy image of the device for the current-switching experiment. Scale bar, 100 μm. **b**, Domain stripes were initially aligned by a magnetic field of 150 mT applied in the *x* direction for 1 s. The pulsed current was then applied in the *x* direction. **c**–**e**, MFM images of a 4 μm × 4 μm region taken after 10 μs current pulses of 10 mA (**c**), 20 mA (**d**) and 25 mA (**e**). **f**, SEM image of the LSMO film with integrated spin-wave nano-stripeline antennas. The current pulse was applied in the *x* direction, parallel to the spin-wave wavevector **k**. Scale bar, 200 nm. **g**–**j**, Spin-wave transmission signals S_{21} (excited at antenna 1 and detected at antenna 2) were measured by the VNA at the initial state (**g**), and after current pulses of 10 mA (**h**), 20 mA (**i**) and 25 mA (**j**). Domain stripes were switched along the *y* direction by a 25 mA current pulse and as a result the spin-wave transmission was switched off.

Conclusions

We have observed the AFM-type spin-wave propagation in LSMO thin films of periodically coupled nanostripe domains with perpendicular magnetic anisotropy. The high-frequency spin waves can propagate at zero bias field over longer distances than low-frequency spin waves. The micromagnetic simulations indicate that these high-frequency spin waves mainly propagate in the domain volume, rather than being localized in the domain wall. The group velocity of the AFM-type spin waves is estimated to be 2.6 km s^{-1}. The spin-wave dispersion is theoretically modelled considering spin-wave propagation along antiparallel coupled domains. Angular dependence measurements indicate that such spin waves tend to propagate along the domain stripes. The domain stripe alignment is experimentally proved to be reprogrammable by applying an electrical current. Our results demonstrate that the periodic antiparallel nanostripe domains can be used to control spin-wave propagation with an electrical current and hence offer great versatility and the possibility to reconfigurable spin-wave devices[19].

Online content

Any methods, additional references, Nature Research reporting summaries, source data, extended data, supplementary information, acknowledgements, peer review information; details of author contributions and competing interests; and statements of data and code availability are available at https://doi.org/10.1038/s41565-019-0429-7.

Received: 29 October 2018; Accepted: 13 March 2019;

References

1. Chumak, A. V., Vasyuchka, V. I., Serga, A. A. & Hillebrands, B. Magnon spintronics. *Nat. Phys.* **11**, 453–461 (2015).
2. Grundler, D. Spintronics: nanomagnonics around the corner. *Nat. Nanotechnol.* **11**, 407–408 (2016).
3. Demidov, V. E. et al. Magnetization oscillations and waves driven by pure spin currents. *Phys. Rep.* **673**, 1–31 (2017).
4. Yu, H., Xiao, J. & Pirro, P. Magnon spintronics. *J. Magn. Magn. Mater.* **450**, 1–2 (2018).
5. Khitun, A., Bao, M. & Wang, K. L. Magnonic logic circuits. *J. Phys. D* **43**, 264005 (2010).
6. Holländer, R. B., Müller, C., Schmalz, J., Gerken, M. & McCord, J. Magnetic domain walls as broadband spin wave and elastic magnetisation wave emitters. *Sci. Rep.* **8**, 13871 (2018).
7. Haldar, A., Kumar, D. & Adeyeye, A. O. A reconfigurable waveguide for energy-efficient transmission and local manipulation of information in a nanomagnetic device. *Nat. Nanotechnol.* **11**, 437–443 (2016).
8. Wagner, K. et al. Magnetic domain walls as reconfigurable spin-wave nanochannels. *Nat. Nanotechnol.* **11**, 432–436 (2016).
9. Jungwirth, T., Marti, X., Wadley, P. & Wunderlich, J. Antiferromagnetic spintronics. *Nat. Nanotechnol.* **11**, 231–241 (2016).
10. Baltz, V. et al. Antiferromagnetic spintronics. *Rev. Mod. Phys.* **90**, 015005 (2018).
11. Kampfrath, T. et al. Coherent terahertz control of antiferromagnetic spin waves. *Nat. Photon.* **5**, 31–34 (2010).
12. Caspers, C., Gandhi, V. P., Magrez, A., Rijk, E. D. & Ansermet, J. Sub-terahertz spectroscopy of magnetic resonance in $BiFeO_3$ using a vector network analyzer. *Appl. Phys. Lett.* **108**, 241109 (2016).
13. Duine, R. A., Lee, K.-J., Parkin, S. S. P. & Stiles, M. D. Synthetic antiferromagnetic spintronics. *Nat. Phys.* **14**, 217–219 (2018).
14. Gruenberg, P., Schreiber, R., Pang, Y., Brodsky, M. B. & Sowers, H. Layered magnetic structures: evidence for antiferromagnetic coupling of Fe layers across Cr interlayers. *Phys. Rev. Lett.* **57**, 2442–2445 (1986).
15. Hillebrands, B. Spin-wave calculations for multilayered structures. *Phys. Rev. B* **41**, 530–540 (1990).
16. Topp, J., Heitmann, D., Kostylev, M. P. & Grundler, D. Making a reconfigurable artificial crystal by ordering bistable magnetic nanowires. *Phys. Rev. Lett.* **104**, 207205 (2010).
17. Ding, J., Kostylev, M. P. & Adeyeye, A. O. Magnonic crystal as a medium with tunable disorder on a periodical lattice. *Phys. Rev. Lett.* **107**, 047205 (2011).
18. Tacchi, S. et al. Analysis of collective spin-wave modes at different points within the hysteresis loop of a one-dimensional magnonic crystal comprising alternative-width nanostripes. *Phys. Rev. B* **82**, 184408 (2010).
19. Grundler, D. Reconfigurable magnonics heats up. *Nat. Phys.* **11**, 438–441 (2015).
20. Wang, J. et al. Nanoscale control of stripe-ordered magnetic domain walls by vertical spin transfer torque in $La_{0.67}Sr_{0.33}MnO_3$ film. *Appl. Phys. Lett.* **112**, 072408 (2018).
21. Magaraggia, R. et al. Probing $La_{0.7}Sr_{0.3}MnO_3$ multilayers via spin wave resonances. *Phys. Rev. B* **84**, 104441 (2011).
22. Yang, S.-H., Ryu, K.-S. & Parkin, S. S. P. Domain-wall velocities of up to 750 m s^{-1} driven by exchange-coupling torque in synthetic antiferromagnets. *Nat. Nanotechnol.* **10**, 221–226 (2015).
23. Kim, K.-J. et al. Fast domain wall motion in the vicinity of the angular momentum compensation temperature of ferrimagnets. *Nat. Mater.* **16**, 1187–1191 (2017).

24. Woo, S. et al. Observation of room-temperature magnetic skyrmions and their current-driven dynamics in ultrathin metallic ferromagnets. *Nat. Nanotechnol.* **15**, 501–506 (2016).
25. Wang, J. et al. Magnetic domain-wall motion twisted by nanoscale probe-induced spin transfer. *Phys. Rev. B* **90**, 224407 (2014).
26. Steenbeck, K. & Hiergeist, R. Magnetic anisotropy of ferromagnetic $La_{0.7}(Sr, Ca)_{0.3}MnO_3$ epitaxial films. *Appl. Phys. Lett.* **75**, 1778–1780 (1999).
27. Bakaul, S. R., Hu, W., Wu, T. & Kimura, T. Intrinsic domain-wall resistivity in half-metallic manganite thin films. *Phys. Rev. B* **86**, 184404 (2012).
28. Vlaminck, V. & Bailleul, M. Current-induced spin-wave Doppler shift. *Science* **322**, 410–413 (2008).
29. Neusser, S. et al. Anisotropic propagation and damping of spin waves in a nanopatterned antidot lattice. *Phys. Rev. Lett.* **105**, 067208 (2010).
30. Yu, H. et al. Magnetic thin-film insulator with ultra-low spin wave damping for coherent nanomagnonics. *Sci. Rep.* **4**, 6848 (2014).
31. Choi, S., Lee, K.-S., Guslienko, K. Y. & Kim, S.-K. Strong radiation of spin waves by core reversal of a magnetic vortex and their wave behaviors in magnetic nanowire waveguides. *Phys. Rev. Lett.* **98**, 087205 (2007).
32. Camara, I. S. et al. Magnetization dynamics of weak stripe domains in Fe–N thin films: a multitechnique complementary approach. *J. Phys. Condens. Matter* **29**, 465803 (2017).
33. Macke, S. & Goll, D. Transmission and reflection of spin waves in the presence of Néel walls. *J. Phys. Conf. Ser.* **200**, 042015 (2010).
34. Hämäläinen, S. J., Madami, M., Qin, H., Gubbiotti, G. & van Dijken, S. Control of spin-wave transmission by a programmable domain wall. *Nat. Commun.* **9**, 4853 (2018).
35. Huber, R. et al. Reciprocal Damon–Eshbach-type spin wave excitation in a magnonic crystal due to tunable magnetic symmetry. *Appl. Phys. Lett.* **102**, 012403 (2013).
36. Daniels, M. W., Guo, W., Stocks, G. M., Xiao, D. & Xiao, J. Spin-transfer torque induced spin waves in antiferromagnetic insulators. *New J. Phys.* **17**, 103039 (2015).
37. Legrand, W. et al. Hybrid chiral domain walls and skyrmions in magnetic multilayers. *Sci. Adv.* **4**, 0415 (2018).
38. Lee, J. M. et al. All-electrical measurement of interfacial Dzyaloshinskii–Moriya interaction using collective spin-wave dynamics. *Nano Lett.* **16**, 62–67 (2016).
39. Gurevich, A. G. & Melkov, G. A. *Magnetization Oscillations and Waves* (CRC, 1996).
40. Stancil, D. D. & Prabhakar, A. *Spin Waves: Theory and Applications* (Springer, 2009).
41. Kalinikos, B. A. & Slavin, A. N. Theory of dipole-exchange spin wave spectrum for ferromagnetic films with mixed exchange boundary conditions. *J. Phys. C* **19**, 7013–7033 (1986).
42. Kronseder, M., Buchner, M., Bauer, H. G. & Back, C. H. Dipolar-energy-activated magnetic domain pattern transformation driven by thermal fluctuations. *Nat. Commun.* **4**, 2054 (2013).
43. Conca, A. et al. Low spin-wave damping in amorphous $Co_{40}Fe_{40}B_{20}$ thin films. *J. Appl. Phys.* **113**, 213909 (2013).
44. Hämäläinen, S. J., Brandl, F., Franke, K. J. A., Grundler, D. & van Dijken, S. Tunable short-wavelength spin-wave emission and confinement in anisotropy-modulated multiferroic heterostructures. *Phys. Rev. Appl.* **8**, 014020 (2017).
45. Slonczewski, J. C. Current-driven excitation of magnetic multilayers. *J. Magn. Magn. Mater.* **159**, L1–L7 (1996).
46. Yan, P., Wang, X. S. & Wang, X. R. All-magnonic spin-transfer torque and domain wall propagation. *Phys. Rev. Lett.* **107**, 177207 (2011).
47. Miron, I. M. et al. Perpendicular switching of a single ferromagnetic layer induced by in-plane current injection. *Nature* **476**, 189–194 (2011).
48. Manchon, A., Koo, H. C., Nitta, J., Frolov, S. M. & Duine, R. A. New perspectives for Rashba spin–orbit coupling. *Nat. Mater.* **14**, 871–882 (2015).
49. Sadovnikov, A. V. et al. Magnon straintronics: reconfigurable spin-wave routing in strain-controlled bilateral magnetic stripes. *Phys. Rev. Lett.* **120**, 257203 (2018).
50. Tacchi, S. et al. Rotatable magnetic anisotropy in a $Fe_{0.8}Ga_{0.2}$ thin film with stripe domains: dynamics versus statics. *Phys. Rev. B* **89**, 024411 (2011).

Acknowledgements

The authors thank J. Hu, K. Wagner and H. Schultheiss for discussions. The authors also acknowledge support from NSF China under grants nos. 11674020, 11444005, U1801661 and 51788104, 111 Talent Program B16001 and the Ministry of Science and Technology of China MOST no. 2016YFA0300802. The work in Beijing Normal University is supported by the National Key Research and Development Program of China through contract no. 2016YFA0302300. J.D. and M.W. were supported by the US National Science Foundation (EFMA-1641989) and the US Department of Energy, Office of Science, Basic Energy Sciences (DE-SC0018994). J.X. is supported by NSF China under grant no. 11722430.

Author contributions

J.X., Jinxing Z. and H.Y. conceived and designed the experiments. S.W., Y.Z. and Jinxing Z. provided the LSMO films. J.D. and M.W. characterized the films with SQUID and FMR techniques. C. Liu, Jianyu Z., J.C. and H.Y. designed and fabricated the spin-wave devices. J.M., S.W., Y.Z., Jinxing Z. and C.-W.N. conducted the MFM measurements. Y.S., C. Liu, P.G. and D.Y. conducted the transmission electron microscopy characterization. C. Liu, Jianyu Z., J.C. and H.Y. performed the spin-wave measurements. S.W., C. Liu, Jianyu Z., S.T. and H.Y. conducted the current-control experiments. S.W., P.L., C. Li and Y.J. fabricated the eight-terminal device for current-switching experiments. J.C., Jianyu Z., C. Liu and H.Y. analysed the data. R.D. performed the theoretical modelling. C. Liu, H.W. and J.C. performed the micromagnetic simulations. Jinxing Z. and H.Y. supervised the experimental study. H.Y., J.C., C. Liu and Jianyu Z. wrote the paper and the Supplementary Information.

Competing interests

The authors declare no competing interests.

Additional information

Supplementary information is available for this paper at https://doi.org/10.1038/s41565-019-0429-7.

Reprints and permissions information is available at www.nature.com/reprints.

Correspondence and requests for materials should be addressed to J.Z. or H.Y.

Journal peer review information: *Nature Nanotechnology* thanks Marco Madami, Markus Münzenberg and other anonymous reviewer(s) for their contribution to the peer review of this work.

Methods

Sample preparation. LSMO thin films (~150 nm) were grown on a (001)-oriented LAO single-crystal substrate by pulsed laser deposition, at an ambient temperature of 780 °C under 25 Pa oxygen pressure. A KrF excimer laser with a wavelength of 248 nm, repetition rate of 5 Hz and energy density of 1.5 J cm^{-2} was used. After deposition, the sample was annealed at 780 °C under 1×10^5 Pa oxygen pressure for 10 min, and then slowly cooled to room temperature at a cooling rate of 5 °C min^{-1}.

Magnetic force microscopy. The magnetic domain structures of the sample were observed by scanning probe microscopy (Variable Field Module 3 (VFM), Infinity, Asylum Research), using a CoCr (50) coated magnetic tip with a force constant of 2 N m^{-1} and resonant frequency of 70 kHz (ASYMFM, Asylum Research). We first imaged the MFM micrographs at zero field, then imaged the domain patterns with applied in-plane magnetic fields and finally took the MFM images again at zero field to see the evolution of the domain structures.

Micromagnetic simulations. The simulations were conducted based on the OOMMF program (http://math.nist.gov/oommf). The simulated area of the LSMO film was 4 μm × 1 μm ($x\times y$) with thickness of 150 nm (z). We assumed a saturation magnetization of $M_s = 307$ kA m^{-1}, exchange constant of $\lambda_{ex} = 1.37\times10^{-16}$ m^2, effective magnetic anisotropy energy of $K = -1.5\times10^4$ J m^{-3} and damping constant of $\alpha = 0.05$. The unit cell (mesh) used in the simulations was 5 nm × 5 nm × 10 nm ($x\times y\times z$). A 100-nm-wide excitation area was set in the middle of the LSMO film. An external static magnetic field was applied in the x direction. The oscillating magnetic field for excitation is defined as H_0 sin(2π × 100 GHz(t−100.1 ps))/(2π × 100 GHz(t−100.1 ps)), where $H_0 = 10$ mT and t indicates time (in ps), and the minimized energy of the simulated structure yields the magnetization ground state. The magnetization dynamics was simulated with equal time intervals of 40 ps starting from the ground state. The frequency-dependent results as shown in Fig. 2 were obtained after a fast Fourier transform of the simulated time-domain magnetization oscillation.

Spin-wave spectroscopy. Spin-wave transmission was measured with two identical CPWs integrated on top of the LSMO thin film for excitation and detection. An in-plane external magnetic field was applied perpendicular to the CPWs while the microwave current was injected from the VNA into the CPWs through the microwave probes. Spin waves were excited in the LSMO film by the alternating electromagnetic field induced by the signal line of the CPWs and propagated from one CPW to the other. By extracting the S_{21} parameter from VNA, spin-wave transmission can be obtained from CPW1 to CPW2, and S_{21} from CPW2 to CPW1. The spin-wave reflection measurements were conducted by placing the LSMO thin film face down onto a large CPW prepared on a silicon wafer. The CPW consisted of one signal line and two ground lines (50 μm wide and spacing of 50 μm). Under the in-plane external magnetic field perpendicular to the CPW, microwave current was injected from the VNA through a three-pitch microwave probe. The wavevector **k** of the flip-chip CPW was almost zero (calculated by Fourier transformation).

Data availability

The authors declare that the main data supporting the findings of this study are available within the article and its Supplementary Information. Extra data are available from the corresponding authors upon reasonable request.